

4D Synchronized Fields: Motion-Language Gaussian Splatting for Temporal Scene Understanding

Mohamed Rayan Barhdadi¹, Samir Abdaljalil¹, Rasul Khanbayov², Erchin Serpedin¹, and Hasan Kurban²

¹ Texas A&M University

² Hamad Bin Khalifa University

 Available_soon

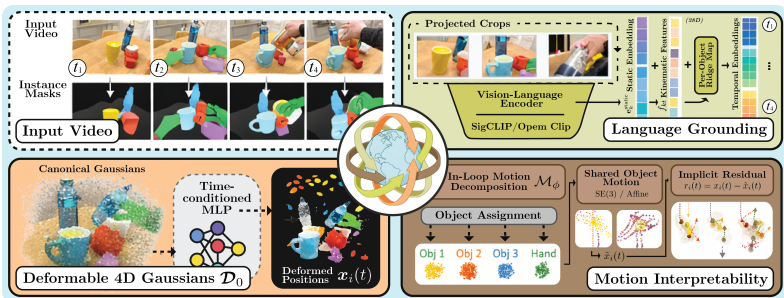


Fig. 1: **4D Synchronized Fields** learns a deformable 4D Gaussian scene whose per-Gaussian trajectories are decomposed in-loop into shared object motion plus implicit residuals. The resulting synchronized tracks and kinematics condition an object-time language field, trained from projected object crops and a per-object ridge map, enabling open-vocabulary temporal queries that retrieve both *objects* and *moments*, grounded in learned motion structure.

Abstract. Current 4D representations decouple geometry, motion, and semantics: reconstruction methods discard interpretable motion structure; language-grounded methods attach semantics after motion is learned, blind to how objects move; and motion-aware methods encode dynamics as opaque per-point residuals without object-level organization. We propose **4D Synchronized Fields**, a 4D Gaussian representation that learns object-factored motion in-loop during reconstruction and synchronizes language to the resulting kinematics through a per-object conditioned field. Each Gaussian trajectory is decomposed into shared object motion plus an implicit residual, and a kinematic-conditioned ridge map predicts temporal semantic variation, yielding a single representation in which reconstruction, motion, and semantics are structurally coupled and enabling open-vocabulary temporal queries that retrieve both objects and moments. On HyperNeRF, 4D Synchronized Fields achieves

28.52 dB mean PSNR, the highest among all language-grounded and motion-aware baselines, within 1.5 dB of reconstruction-only methods. On targeted temporal-state retrieval, the kinematic-conditioned field attains 0.884 mean accuracy, 0.815 mean vIoU, and 0.733 mean tIoU, surpassing LangSplat (0.415, 0.304, and 0.262) and 4D LangSplat (0.620, 0.433, and 0.439 respectively). Ablation confirms that kinematic conditioning is the primary driver, accounting for +0.45 tIoU over a static-embedding-only baseline. 4D Synchronized Fields is the only method that jointly exposes interpretable motion primitives and temporally grounded language fields from a single trained representation. Code will be released.

Keywords: 4D Gaussian Splatting, Dynamic Scene Understanding, Object Motion Decomposition, Open-Vocabulary Temporal Queries

1 Introduction

Building faithful representations of the world is a long-standing goal of visual computing, pursued through stages that successively close the gap between what is represented and what the world actually contains. Early work focused on what could be extracted from a single image: edges and local features [37,35], part-based shape models [2,12], and learned hierarchies for recognition at scale [25], yet recognizing *what* is in an image leaves open the question of *where* things are in three dimensions. Multi-view geometry and structure-from-motion [18,46] recovered 3D structure from image collections; neural radiance fields [38] encoded scenes as continuous volumetric functions for photorealistic novel-view synthesis [1,39]; and 3D Gaussian Splatting [22] replaced implicit volumetric queries with explicit, rasterizable primitives at real-time rates.

#1: the world can now be reconstructed and rendered with high fidelity, but the representation is blind to what it depicts.

Language-grounded methods [23,43,59,62,6] attached open-vocabulary semantics to 3D structures. 4D LangSplat [29] and related works [36,20] extended this to temporal representations, but language features are typically distilled *after* motion has been optimized, so the semantic field inherits no structured knowledge of *how* objects move, only a static association with *what* is present.

#2: language grounding lets the representation know *what* it depicts, but it treats motion as a black box and cannot express *how* things move.

Knowing *what* is not enough when the world is not static: objects move, interact, and change state. Deformation-based NeRFs [42,40,41], scene-flow methods [31,15,34], factored space-time representations [14,3], and 4D Gaussian Splatting [57,58,32,30] brought dynamic reconstruction within reach, yet motion is encoded as per-point deformation optimized purely for photometric error, exposing no interpretable object-level structure.

#3: motion-aware methods model dynamics, but motion remains an opaque per-point residual with no object-level structure or semantic coupling.

The absence of object-level structure is not just an engineering limitation; it conflicts with how biological perception is organized. From the first months of life, infants perceive objects as cohesive bodies by attending to how surfaces move, well before relying on appearance [52,53,4], and objects individuated through motion serve as the hubs around which perception, action, and language coalesce [49,50]. World models that must predict, plan, and explain in terms of objects require representations exposing motion as a first-class, interpretable quantity [54,48,17,51].³

#4: closing the loop requires *synchronization*: motion must be factored by object, and semantics must be conditioned on that factored motion, so that reconstruction, language, and dynamics are unified within a single representation.

We present 4D SYNCHRONIZED FIELDS, a 4D scene representation built on the synchronization principle of #4. 4D SYNCHRONIZED FIELDS learns renderable Gaussians while fitting an object-consistent motion model *in-loop* during reconstruction, so that motion structure, object identity, and semantics emerge together rather than being bolted on in sequence.

In summary, our contributions are as follows:

A synchronized 4D scene representation. We propose the first representation that synchronizes reconstruction, object-factored motion, and language within a unified Gaussian representation via staged training: motion structure is learned first, and language is then grounded on the resulting kinematics, culminating the progression of #1 to #3 and instantiating the synchronization principle of #4.

In-loop motion decomposition. Each Gaussian’s trajectory is decomposed into shared object motion (SE(3) or affine) plus an implicit residual, with a residual-adaptive modulation scheme that relaxes regularization on persistently non-rigid Gaussians while leaving the forward renderer unchanged.

Kinematic-conditioned language field. We train a per-object ridge map from a kinematic feature vector to semantic residuals, yielding an object-time embedding field that supports open-vocabulary temporal queries and surpasses existing language-grounded baselines on state retrieval.

Structured temporal scene understanding. The representation produces synchronized object tracks, motion primitives, interaction graphs, and language slots that a multimodal LLM can directly consume at inference time for temporal reasoning, without having entered the training loop or requiring task-specific retraining.

³ We adopt a perception-first viewpoint: the representation is learned from visual supervision; language serves as an interface to the learned structure over space and time. This mirrors developmental findings in which infants first build core object representations from spatiotemporal cues and only later integrate linguistic labels [4,56].

2 Related Work

We organize prior work along four capability axes and assign each a visual marker used consistently throughout the paper, in section headers, method stages, tables, and result discussions: Reconstruction Language grounding Motion structure

Synchronized (ours). No existing method spans all four; 4D SYNCHRONIZED FIELDS is the first to do so within a single trained representation.

3D and 4D reconstruction. ■ NeRFs [38,1,39] and 3D Gaussian Splatting [22] achieve photorealistic novel-view synthesis from static scenes. Dynamic extensions, including deformation-based NeRFs [42,40,41], scene-flow methods [31,15,34], factored representations [14,3], and 4D Gaussian variants [57,58,32,30], optimize deformation for photometric fidelity alone, exposing no interpretable object-level kinematics. 4D SYNCHRONIZED FIELDS constrains this deformation field with an in-loop object-level factorization (§3).

Language-grounded scene representations. ■ Vision-language features [44,60,9] have been distilled into 3D via LERF [23], LangSplat [43], Feature 3DGS [62], and Gaussian Grouping [59]. In dynamic scenes, 4D LangSplat [29] learns dual semantic fields from CLIP and MLLM-generated captions; 4-LEGS [13] and DGD [26] lift features onto dynamic Gaussians. In all cases, language is learned on a frozen deformation backbone with no access to object-level motion. 4D SYNCHRONIZED FIELDS fits motion primitives during reconstruction and conditions language on the resulting kinematics.

Motion and object-centric representations. ■ No existing method imposes a training-time factorization of shared object motion versus per-Gaussian residuals; 4D SYNCHRONIZED FIELDS introduces this *inside* the optimization loop. Foundation-model segmentation [24,45,5] and dense correspondence [10,11,21] provide post-hoc object signals [7,6,20,36] but do not shape the motion representation itself. Motion-graph approaches require skeletal priors; 4D SYNCHRONIZED FIELDS trades part-level granularity for generality via the modular \mathcal{M}_ϕ interface (§5).

Toward synchronized temporal understanding. ■ Multimodal LLMs [27,33], world models [17,51,8], and developmental evidence [4,49,50] all point toward motion-factored object representations as a prerequisite for higher-level reasoning. Concurrent feed-forward approaches [55] trade per-scene fidelity for scalability; 4D SYNCHRONIZED FIELDS is, to our knowledge, the first 4D representation that synchronizes reconstruction, motion, and language within a single trained structure.

3 Method

We describe 4D SYNCHRONIZED FIELDS in five stages: deformable 4D Gaussian reconstruction ■ (§3.1), object assignment ■ (§3.2), in-loop motion decomposition ■ (§3.3), anti-degeneracy objectives with residual-adaptive modulation ■ (§3.4), and a synchronized object-time language field ■ (§3.5). Diagnostics and

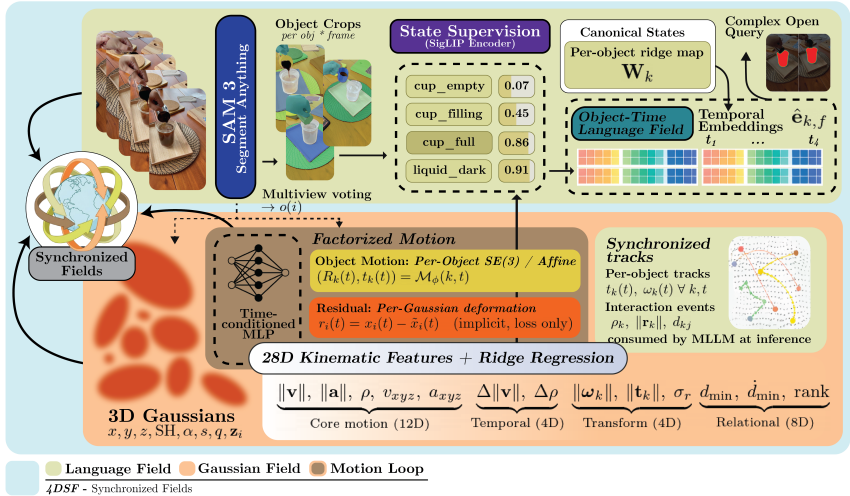


Fig. 2: **Method overview.** A time-conditioned deformation MLP \mathcal{D}_θ predicts per-Gaussian deltas yielding deformed positions $\mathbf{x}_i(t)$. A shared object-motion model \mathcal{M}_ϕ produces per-object transforms yielding object-predicted positions $\tilde{\mathbf{x}}_i(t)$. The residual $\mathbf{r}_i(t) = \mathbf{x}_i(t) - \tilde{\mathbf{x}}_i(t)$ is defined implicitly and used only in regularizers; rendering uses $\mathbf{x}_i(t)$ unchanged. After training, synchronized tracks and 28D kinematic features are extracted and used to fit per-object ridge maps from kinematics to semantic residuals, yielding an object-time language field for open-vocabulary temporal queries; the resulting structured scene description is then leveraged by a multimodal LLM for downstream reasoning.

structured temporal export \blacksquare are described in §3.6. The ordering is deliberate: motion structure must be learned before language can be conditioned on it (§3.5). Colored markers indicate which capability from §1 each stage addresses.

3.1 Preliminaries: Deformable 4D Gaussian Splatting

■ A scene is represented as N anisotropic Gaussians $\{\mathcal{G}_i\}_{i=1}^N$ with canonical mean $\mathbf{x}_i^0 \in \mathbb{R}^3$, rotation \mathbf{q}_i^0 , log-scale \mathbf{s}_i^0 , opacity α_i , and SH color \mathbf{c}_i , rendered via alpha-compositing [22]. Each Gaussian carries a learned embedding $\mathbf{z}_i \in \mathbb{R}^D$ that, together with the canonical position and encoded time, conditions a deformation MLP:

$$(\Delta\mathbf{x}_i, \Delta\omega_i, \Delta\ell_i) = \mathcal{D}_\theta(\mathbf{x}_i^0, \mathbf{z}_i, \gamma(t)), \quad (1)$$

where $\gamma(t)$ is sinusoidal positional encoding. The final layer is zero-initialized so that training begins from identity deformation (architecture in Appendix A). Deformed parameters at time t ($\mathbf{q}(\cdot)$ denotes axis-angle to unit-quaternion con-

version):

$$\mathbf{x}_i(t) = \mathbf{x}_i^0 + \Delta \mathbf{x}_i(t), \quad (2)$$

$$\mathbf{q}_i(t) = \text{normalize}(\mathbf{q}(\Delta \boldsymbol{\omega}_i(t)) \otimes \mathbf{q}_i^0), \quad (3)$$

$$\mathbf{s}_i(t) = \exp(\log \mathbf{s}_i^0 + \Delta \boldsymbol{\ell}_i(t)). \quad (4)$$

Training uses the standard photometric loss

$$\mathcal{L}_{\text{rgb}} = \lambda_1 \|\hat{\mathbf{F}} - \mathbf{F}\|_1 + \lambda_{\text{dssim}} \text{DSSIM}(\hat{\mathbf{F}}, \mathbf{F}) \quad (5)$$

with standard densification [22].

3.2 Object Assignment from External Masks

■ The motion decomposition (§3.3) requires each Gaussian to be assigned to an object. We obtain per-frame instance masks from an external segmenter (SAM 3 [5] in our experiments), though the design is compatible with any instance segmenter. Each Gaussian i is projected into every training frame; if it lands on a labeled pixel, one vote is added to that label. Aggregating votes yields a matrix $\mathbf{V} \in \mathbb{R}^{N \times (K+1)}$; each Gaussian is assigned to its majority label subject to minimum-vote and minimum-consistency filters (thresholds in Appendix A). We write $o(i) \in \{0, \dots, K-1\}$ for the resulting assignment. Multiview voting suppresses per-frame segmentation noise by requiring consistent labels across many views; we validate assignment quality via a shuffle test in Appendix C.

3.3 In-Loop Motion Decomposition

■ Given object assignments from §3.2, 4D SYNCHRONIZED FIELDS decomposes each Gaussian’s predicted motion into (a) a shared, object-consistent transform and (b) an implicit per-Gaussian residual, *without altering the forward renderer*. **Shared object-motion model** \mathcal{M}_ϕ . A learnable model outputs a rigid or affine transform per object k and time t . In the SE(3) parameterization:

$$(\mathbf{R}_k(t), \mathbf{t}_k(t)) = \mathcal{M}_\phi(k, t), \quad \tilde{\mathbf{x}}_i(t) = \mathbf{R}_{o(i)}(t) \mathbf{x}_i^0 + \mathbf{t}_{o(i)}(t). \quad (6)$$

In the affine variant, $\tilde{\mathbf{x}}_i(t) = (\mathbf{I} + \Delta \mathbf{A}_{o(i)}(t)) \mathbf{x}_i^0 + \mathbf{b}_{o(i)}(t)$. All parameters are initialized near identity (Appendix A).

Implicit residual. The residual is defined from the predictions of \mathcal{D}_θ and \mathcal{M}_ϕ :

$$\mathbf{r}_i(t) = \mathbf{x}_i(t) - \tilde{\mathbf{x}}_i(t). \quad (7)$$

By construction $\mathbf{x}_i(t) = \tilde{\mathbf{x}}_i(t) + \mathbf{r}_i(t)$, so rendering uses $\mathbf{x}_i(t)$ unchanged; the decomposition injects training signal only through the regularizers below.

3.4 Anti-Degeneracy Objectives

■ Because the deformation MLP \mathcal{D}_θ is strictly more expressive than the per-object SE(3) model, it can absorb all motion into residuals unless explicitly constrained. We employ five regularizers to prevent this collapse.

(i) *Residual energy (base form).*

$$\mathcal{L}_{\text{res}} = \frac{1}{N} \sum_{i=1}^N \|\mathbf{r}_i(t)\|_2^2. \quad (8)$$

(ii) *Residual-adaptive modulation.* Gaussians on boundaries or articulated joints carry genuinely non-rigid motion and should not be penalized equally. We track per-Gaussian residual magnitude via EMA ($\eta=0.95$) and compute a modulation weight from the z-scored running average (sigm: logistic sigmoid):

$$m_i = \text{sigm}\left(\frac{\bar{r}_i - \mu_{\bar{r}}}{\sigma_{\bar{r}} + \varepsilon}\right), \quad \mathcal{L}_{\text{res}}^{\text{mod}} = \frac{1}{N} \sum_{i=1}^N (1 - m_i) \|\mathbf{r}_i(t)\|_2^2. \quad (9)$$

$\mathcal{L}_{\text{res}}^{\text{mod}}$ replaces \mathcal{L}_{res} in the total objective (Eq. 13); the base form is shown for clarity.

(iii) *Rigid-share hinge.* We measure the fraction of motion explained by the shared transform and impose a minimum target τ :

$$\rho(t) = \frac{1}{N} \sum_{i=1}^N \frac{\|\tilde{\mathbf{x}}_i(t) - \mathbf{x}_i^0\|_2}{\|\tilde{\mathbf{x}}_i(t) - \mathbf{x}_i^0\|_2 + \|\mathbf{r}_i(t)\|_2 + \varepsilon}, \quad \mathcal{L}_{\text{share}} = [\max(0, \tau - \rho(t))]^2. \quad (10)$$

The hinge is one-sided, active only when $\rho < \tau$, so scenes that naturally exceed τ incur no penalty.

(iv) *Velocity coherence.* Aligns per-Gaussian and object-level velocity (t^- : previous frame):

$$\mathcal{L}_{\text{vel}} = \frac{1}{N} \sum_{i=1}^N \|(\Delta \mathbf{x}_i(t) - \Delta \mathbf{x}_i(t^-)) - (\tilde{\mathbf{x}}_i(t) - \tilde{\mathbf{x}}_i(t^-))\|_2^2. \quad (11)$$

(v) *Temporal smoothness.* Penalizes high-frequency variation in the axis-angle $\boldsymbol{\omega}_k(t)$ and translation $\mathbf{t}_k(t)$ of \mathcal{M}_ϕ between consecutive frames:

$$\mathcal{L}_{\text{smooth}} = \frac{1}{K} \sum_{k=0}^{K-1} \left(\|\boldsymbol{\omega}_k(t) - \boldsymbol{\omega}_k(t^-)\|_2^2 + \|\mathbf{t}_k(t) - \mathbf{t}_k(t^-)\|_2^2 \right). \quad (12)$$

Total objective:

$$\mathcal{L} = \mathcal{L}_{\text{rgb}} + \lambda_{\text{res}} \mathcal{L}_{\text{res}}^{\text{mod}} + \lambda_{\text{share}} \mathcal{L}_{\text{share}} + \lambda_{\text{vel}} \mathcal{L}_{\text{vel}} + \lambda_{\text{smooth}} \mathcal{L}_{\text{smooth}}. \quad (13)$$

Motion losses are activated in stages for stability (schedule in Appendix A).

3.5 Synchronized Object-Time Language Field

■ The insight driving this stage is that an object’s kinematics predict its semantic state: how it moves reveals what it is doing. We build a semantic embedding field over objects and time from three ingredients: visual crop embeddings, a static appearance anchor, and a per-object ridge map from kinematics to semantic residuals. The language field is trained on a frozen motion checkpoint rather than jointly with rendering; joint training would couple the high-dimensional SigLIP embedding space to the photometric loss, destabilizing both objectives. This staged design lets each component converge independently while kinematic conditioning ensures that language is structurally informed by motion.

Visual observations. For each object k visible in frame f , we project its Gaussians into the image, extract a bounding-box crop, and encode it:

$$\mathbf{e}_{k,f}^{\text{obs}} = \text{norm}(E_{\text{img}}(\text{crop}(k, f))) \in \mathbb{R}^{D_e}, \quad (14)$$

using SigLIP [60] by default; we prefer SigLIP over CLIP/OpenCLIP because its sigmoid-based contrastive loss produces better-calibrated per-object similarities for the cross-object scoring in Eq. 17.

Static embedding. The appearance anchor is the normalized mean over observed frames: $\mathbf{e}_k^{\text{static}} = \text{norm}\left(\frac{1}{|\mathcal{F}_k|} \sum_{f \in \mathcal{F}_k} \mathbf{e}_{k,f}^{\text{obs}}\right)$.

Per-object ridge map. For each object-time pair (k, f) we construct a 28-dimensional kinematic feature vector $\mathbf{f}_{k,f} \in \mathbb{R}^{28}$ encoding core motion, temporal derivatives, transform diagnostics, and relational context (full breakdown in Appendix B). We standardize features per object and append a bias term to obtain $\tilde{\mathbf{f}}_{k,f} \in \mathbb{R}^{29}$, then fit a per-object ridge regression from kinematic features to semantic residuals $\Delta \mathbf{e}_{k,f} = \mathbf{e}_{k,f}^{\text{obs}} - \mathbf{e}_k^{\text{static}}$:

$$\mathbf{W}_k = \arg \min_{\mathbf{W}} \sum_{(k,f) \in \mathcal{O}_k} \|\tilde{\mathbf{f}}_{k,f}^\top \mathbf{W} - \Delta \mathbf{e}_{k,f}\|_2^2 + \lambda \|\mathbf{W}\|_F^2. \quad (15)$$

This admits a closed-form solution and is fit independently per object.

Predicted embedding and blending. For all object-time pairs:

$$\hat{\mathbf{e}}_{k,f} = \text{norm}\left(\mathbf{e}_k^{\text{static}} + \tilde{\mathbf{f}}_{k,f}^\top \mathbf{W}_k\right). \quad (16)$$

Where observations exist, we blend prediction and observation ($\beta=0.65$); otherwise the prediction is used directly. A temporal EMA pass ($\gamma=0.15$) smooths the result; under prolonged occlusion, the kinematic prediction $\hat{\mathbf{e}}_{k,f}$ serves as the sole embedding, gracefully degrading to motion-only semantics.

Open-vocabulary querying. For query q with embedding $\mathbf{e}_q = \text{norm}(E_{\text{txt}}(q))$, we score each object via a mixture of static and temporal similarity:

$$S(k; q) = w_s \langle \mathbf{e}_k^{\text{static}}, \mathbf{e}_q \rangle + w_t \max_f \langle \mathbf{e}_{k,f}^{\text{sync}}, \mathbf{e}_q \rangle, \quad (17)$$

with $w_s=0.35$ and $w_t=0.65$.

3.6 Diagnostics and Structured Export

■ The decomposition yields four built-in diagnostics (residual mean, rigid-share ratio, assignment shuffle test, and per-object motion variance), detailed in Appendix C. After training, 4D SYNCHRONIZED FIELDS exports a structured scene description comprising object slots, per-frame tracks with full kinematics, pairwise interaction events, and synchronized language embeddings (Appendix D). This description is consumed at inference time by a multimodal LLM through a dedicated prompt layer (Appendix G).

4 Experiments

We evaluate 4D SYNCHRONIZED FIELDS along three axes: reconstruction fidelity, motion factorization quality, and language synchronization.

4.1 Experimental Setup

Datasets. We evaluate on **HyperNeRF** [41] (6 scenes) and **Neu3D** [28].

Metrics. Reconstruction: PSNR, SSIM, LPIPS [61]. Motion: rigid-share ratio ρ , residual mean. Language: query-state accuracy (Acc), volumetric IoU (vIoU), temporal interval IoU (tIoU).

Baselines. *Language-grounded:* 4D LangSplat [29], LangSplat [43], LEGaussians [47], LERF [23]; *reconstruction-only:* Deformable 3DGS [58], SC-GS [19], 4DGaussians [57], 3DGS [22]; *motion-aware:* MotionGS [16]. All methods are evaluated on a held-out test split at matched resolution under a controlled protocol (details in Table 1 caption and Appendix A). 4-LEGS [13] and DGD [26] are discussed in §2 but excluded from Tables 1 and 2 because neither provides public code or pre-trained models on HyperNeRF at the time of submission. Motion-Blender GS targets skeletal scenes and does not report on this benchmark.

Architecture and runtime. \mathcal{D}_θ is a 4-layer MLP (128-dim hidden, 0.13M params); \mathcal{M}_ϕ stores per-object per-frame SE(3) parameters (6KT floats, <0.01M). Total training: ~41 min per scene on a single A100 (30k backbone iterations + 20k motion decomposition); the language field (closed-form ridge) adds <1 min. The motion decomposition adds ~12% wall-time overhead relative to the backbone alone, with negligible memory cost since \mathcal{M}_ϕ operates on object centroids rather than all N Gaussians.

4.2 Reconstruction Quality

Table 1 presents a controlled comparison. Among language-grounded methods, 4D SYNCHRONIZED FIELDS achieves the highest mean PSNR (28.52 dB vs. 25.58 dB for 4D LangSplat) and leads on all four metrics. Reconstruction-only methods score higher because they optimize exclusively for photometric fidelity with no structural constraints. Despite five additional regularizers (§3.4), the

gap to the recon-only upper bound (Deformable-3DGS, 30.04 dB) is only 1.5 dB, substantially narrower than the 4.5 dB gap for 4D LangSplat, indicating that the factorization acts as a beneficial inductive bias rather than a reconstruction penalty. All methods use identical held-out frames, resolution, and COLMAP initialization; our method uses SigLIP (no MLLM captions during training), while 4D LangSplat additionally uses MLLM-generated captions as supervision. Runtime and parameter counts are reported in Appendix A.

4.3 Motion Factorization Quality

The factorization achieves rigid-share ratios of 0.41 to 0.53 across scenes (mean $\bar{\rho}=0.472$, mean residual 0.037). Scenes with predominantly rigid motion (split-cookie: 0.528; americano: 0.508) achieve higher rigid share; scenes with significant non-rigid deformation (espresso: 0.411; keyboard: 0.422) have lower rigid share and higher residual, consistent with physical content. No existing dynamic benchmark provides ground-truth per-object SE(3) trajectories, so motion quality is assessed via internal diagnostics. The shuffle test (Appendix C) confirms object-specificity: permuting labels increases residual energy by $1.52\times$. Across scenes, 23% of Gaussians have $m_i > 0.5$, concentrated on boundaries and articulated regions as expected.

4.4 Language Synchronization

Table 2 reports targeted temporal-state retrieval on four HyperNeRF scenes with human-annotated per-frame state labels and explicit query-to-state mapping heuristics designed to isolate temporal reasoning precision (e.g., americano: “luminous-liquid phase”; espresso: “liquid above midpoint”). For each state query the method returns a binary per-frame activation; Acc, vIoU, and tIoU are computed against ground-truth frame intervals (Appendix F). 4D SYNCHRONIZED FIELDS achieves 0.884 mean Acc (vs. 0.415 for LangSplat, 0.620 for 4D LangSplat), 0.815 mean vIoU (vs. 0.304 and 0.433), and 0.733 mean tIoU (vs. 0.262 and 0.439). The largest gains are on americano ($\Delta\text{Acc} = +0.62$, $\Delta\text{vIoU} = +0.86$) and espresso ($\Delta\text{Acc} = +0.30$, $\Delta\text{vIoU} = +0.43$), where state transitions are tightly coupled to object motion; the gap is narrower on chickchicken, where state changes are partly appearance-driven. Figure 3 shows qualitative temporal localization on two challenging queries.

4.5 Ablation Studies

Reconstruction backbone. Tables 3 and 4 present component and pipeline ablations. Removing opacity reset costs -0.08 dB; further delaying densification costs -0.24 dB total. The full pipeline recovers $+0.87$ dB over the backbone alone (Table 4).

Motion decomposition components. Removing \mathcal{M}_ϕ eliminates the factorization ($\bar{\rho} \rightarrow 0$) and increases residual energy by 32%, yet PSNR is unchanged

Table 1: **Novel-view reconstruction on HyperNeRF** (held-out 4D LangSplat test split, $2\times$ resolution). Best per category in *darker* shade; our results **bold**. Categories are **not directly comparable**: reconstruction-only methods (orange) optimize purely for pixel fidelity with no motion or language objectives. Despite additional structural constraints, our method (blue) closes to within 1.5dB of the recon-only upper bound while **outperforming all language-grounded and motion-aware baselines**.

		Ours (synchronized)	Language-grounded	Reconstruction-only	Motion-aware			
Metric	Method	americano	chickchicken	espresso	keyboard	split-cookie	torchocolate	Mean
PSNR \uparrow	Ours	29.23	27.49	27.44	29.67	32.70	24.59	28.52
	4D LangSplat	28.00	26.46	19.15	27.13	27.70	25.02	25.58
	LangSplat	16.57	17.24	16.71	16.43	16.65	16.57	16.69
	LeGaussians	16.48	17.18	16.55	16.48	16.77	16.57	16.67
	LERF	21.13	19.97	24.39	24.44	20.82	20.79	21.92
	Deformable-3DGS	32.12	28.02	27.11	29.70	34.13	29.18	30.04
	SC-GS	31.39	27.66	26.85	29.95	32.97	28.69	29.59
	4DGaussians	28.92	27.07	25.44	28.26	31.10	26.32	27.85
	3DGS	17.33	17.60	16.97	16.66	17.36	16.78	17.12
	MotionGS	29.62	27.26	26.26	28.43	30.03	27.20	28.13
SSIM \uparrow	Ours	0.91	0.80	0.92	0.92	0.94	0.87	0.89
	4D LangSplat	0.87	0.78	0.85	0.87	0.81	0.84	0.84
	LangSplat	0.63	0.73	0.80	0.72	0.68	0.76	0.72
	LeGaussians	0.63	0.73	0.80	0.72	0.68	0.75	0.72
	LERF	0.67	0.74	0.88	0.83	0.60	0.75	0.75
	Deformable-3DGS	0.94	0.84	0.92	0.92	0.95	0.91	0.91
	SC-GS	0.93	0.84	0.92	0.92	0.94	0.90	0.91
	4DGaussians	0.86	0.82	0.90	0.89	0.88	0.86	0.87
	3DGS	0.67	0.74	0.81	0.74	0.71	0.76	0.74
	MotionGS	0.91	0.83	0.91	0.90	0.91	0.89	0.89
LPIPS-A \downarrow	Ours	0.097	0.291	0.145	0.101	0.080	0.205	0.153
	4D LangSplat	0.163	0.330	0.203	0.165	0.294	0.267	0.237
	LangSplat	0.589	0.606	0.568	0.627	0.579	0.614	0.597
	LeGaussians	0.588	0.606	0.564	0.627	0.580	0.614	0.596
	LERF	0.141	0.293	0.156	0.165	0.213	0.290	0.210
	Deformable-3DGS	0.062	0.224	0.145	0.087	0.056	0.150	0.121
	SC-GS	0.069	0.253	0.152	0.090	0.066	0.184	0.136
	4DGaussians	0.153	0.295	0.181	0.188	0.184	0.300	0.217
	3DGS	0.685	0.666	0.596	0.671	0.669	0.654	0.657
	MotionGS	0.100	0.290	0.183	0.118	0.121	0.227	0.173
LPIPS-V \downarrow	Ours	0.161	0.372	0.249	0.205	0.144	0.284	0.236
	4D LangSplat	0.253	0.433	0.323	0.292	0.373	0.354	0.338
	LangSplat	0.586	0.613	0.561	0.610	0.597	0.574	0.590
	LeGaussians	0.587	0.615	0.560	0.609	0.595	0.575	0.590
	LERF	0.141	0.293	0.156	0.165	0.213	0.290	0.210
	Deformable-3DGS	0.113	0.320	0.249	0.180	0.104	0.225	0.198
	SC-GS	0.121	0.353	0.264	0.186	0.116	0.258	0.216
	4DGaussians	0.249	0.393	0.291	0.279	0.257	0.362	0.305
	3DGS	0.618	0.638	0.569	0.630	0.625	0.592	0.612
	MotionGS	0.158	0.381	0.280	0.210	0.182	0.293	0.251

(+0.07 dB), confirming interpretable structure at zero reconstruction cost. Removing modulation degrades PSNR (-0.11 dB) and inflates residuals by 52%. Removing the hinge collapses $\bar{\rho}$ by 37%. The staged loss activation is essential:

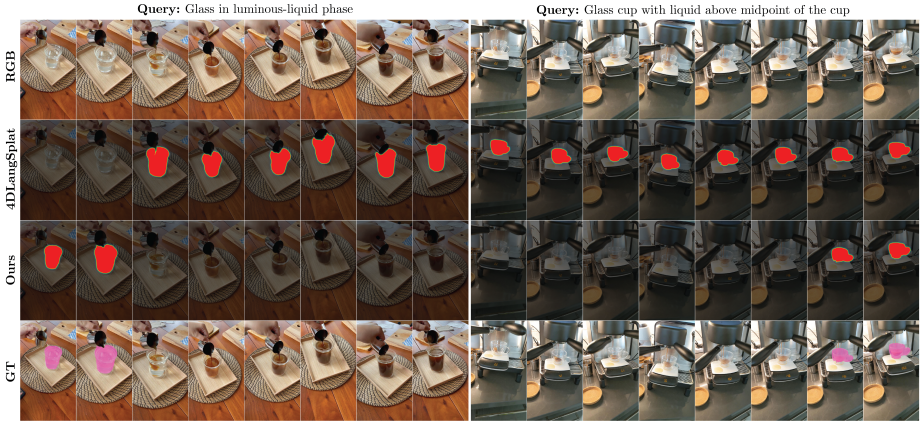


Fig. 3: **Targeted temporal-state retrieval** on americano (left: “glass in luminous-liquid phase”) and espresso (right: “glass cup with liquid above midpoint”). Rows: RGB input, 4D LangSplat activation, 4D SYNCHRONIZED FIELDS activation, ground truth. 4D LangSplat activates broadly across the temporal extent; 4D SYNCHRONIZED FIELDS produces tighter activations aligned with ground-truth intervals, reflecting kinematic conditioning’s sensitivity to motion-correlated state transitions.

Table 2: **Targeted temporal-state retrieval** on four HyperNeRF scenes with human-annotated state labels. Best per metric in *darker* shade; our results **bold**.

		Ours (synchronized)	Language-grounded baselines			
Metric	Method	americano	chickchicken	espresso	split-cookie	Mean
Acc \uparrow	Ours	1.000	0.717	0.951	0.868	0.884
	LangSplat	0.885	0.500	0.086	0.189	0.415
	4D LangSplat	0.385	0.630	0.654	0.811	0.620
vIoU \uparrow	Ours	1.000	0.683	0.810	0.767	0.815
	LangSplat	0.700	0.395	0.000	0.122	0.304
	4D LangSplat	0.135	0.541	0.378	0.677	0.433
tIoU \uparrow	Ours	0.929	0.418	0.821	0.762	0.733
	LangSplat	0.777	0.220	0.000	0.052	0.262
	4D LangSplat	0.149	0.290	0.592	0.724	0.439

simultaneous activation causes $\bar{\rho}$ to plateau below 0.15. The target $\tau = 0.35$ is fixed across all scenes; the one-sided hinge means scenes exceeding it (split-cookie: $\rho=0.53$) incur zero penalty.

Kinematic conditioning. Table 5 isolates the effect of kinematic conditioning by comparing the full ridge-map pipeline against a static-embedding-only

Table 3: Component ablation (4-scene mean). $\bar{\rho}$: rigid-share ratio; Res.: residual L2.

Variant	Δ PSNR	Δ SSIM	$\bar{\rho}$	Res.
Ours	28.52	.89	.472	.037
<i>Backbone (no motion decomp.)</i>				
w/o op. reset	-0.08	-0.000		
Low reset	-0.05	+0.000		
w/o reset+late den.	-0.24	-0.002		
<i>Motion decomposition</i>				
w/o \mathcal{M}_ϕ	+0.07	+0.000	.000	+0.002
w/o modulation	-0.11	-0.002	.330	+0.004
w/o share hinge	+0.03	-0.007	.209	-0.003

Table 4: Pipeline stages (4-scene mean). \checkmark = capability.

Stage	PSNR	Mot.	Lang.	Exp.
Ours	28.52	\checkmark	\checkmark	\checkmark
Backbone only	27.59	\times	\times	\times
+ motion	28.46	\checkmark	\times	\times
+ language	28.46	\checkmark	\checkmark	\checkmark

Table 5: Kinematic conditioning ablation (4-scene mean). Removing the ridge map from kinematics to semantics.

Variant	Acc	vIoU	tIoU
Full (ridge + kinematics)	0.884	0.815	0.733
Static embedding only	0.626	0.446	0.279
Δ (drop)	-0.258	-0.369	-0.453

baseline. Removing kinematic conditioning drops mean Acc from 0.884 to 0.626 (-0.258), vIoU from 0.815 to 0.446 (-0.369), and tIoU from 0.733 to 0.279 (-0.453), more than halving temporal localization quality. The largest drops are on espresso (Δ Acc = -0.74 , Δ tIoU = -0.60) and americano (Δ vIoU = -0.64 , Δ tIoU = -0.64), both motion-dominated. Even on chickchicken, kinematic conditioning improves tIoU by $+0.31$. This confirms that kinematic features are the primary driver of temporal localization: the static anchor alone cannot distinguish *when* a state holds.

5 Discussion

The reconstruction gap. The 1.5 dB gap to reconstruction-only methods is an explicit tradeoff: five motion regularizers constrain the deformation field toward object-consistent trajectories while leaving the renderer unchanged. That this costs only 1.5 dB (vs. 4.5 dB for 4D LangSplat) suggests the factorization acts as a beneficial inductive bias.

What “synchronized” means. The language field is structurally conditioned on the learned motion decomposition: the 28D kinematic feature vector is computed from \mathcal{M}_ϕ ’s per-object transforms, the rigid-share diagnostic, and the residual statistics. This coupling is stronger than in prior methods, where language is distilled onto a frozen backbone with no access to object-level motion primitives.

The staged design is a stability requirement; the closed-form ridge fit eliminates gradient-based language training.

Object assignment robustness. Multiview majority voting (§3.2) suppresses per-frame segmentation errors by requiring consistent labels across ≥ 3 views. The shuffle test confirms object-specificity ($1.52\times$ residual increase). Systematic mask failures propagate into the factorization, a limitation shared with all methods consuming external masks.

Residual absorption and SE(3) expressiveness. The shared transform captures the dominant rigid component; genuinely non-rigid motion is absorbed by residuals and flagged by modulation (m_i). Across scenes, 23% of Gaussians carry $m_i > 0.5$, concentrated on physically expected regions. Extending to part-based decompositions would refine articulated bodies.

Appearance-driven states. The *chickchicken* result, where the margin is narrowest, reveals that kinematic conditioning provides limited signal when state changes are driven by surface appearance. Fusing MLLM-derived appearance features with the ridge map is a natural extension.

Broader impact. Motion, objects, and language are a coupled system that must be learned as such. The structured export (§3.6) provides the interface that world models, embodied agents, and robotic planners need to reason about dynamic scenes in terms of objects and their state transitions.

6 Limitations and Future Work

(i) Object assignment depends on external masks (SAM 3); *learned dynamic segmentation* is a natural remedy. (ii) The SE(3)/affine transform cannot model articulated bodies; *hierarchical part-based motion* would enable articulated decomposition. (iii) Motion quality is evaluated indirectly; *motion-rich benchmarks* with ground-truth poses and state labels would strengthen evaluation for all methods. (iv) The method is optimization-based (~ 41 min/scene on a single A100). (v) Kinematic conditioning underperforms on appearance-driven state changes; *appearance-kinematic fusion* would address this. (vi) The structured export is consumed post hoc; tighter *world-model integration* is a high-impact direction.

7 Conclusion

We presented 4D Synchronized Fields, a 4D Gaussian representation that decomposes per-Gaussian motion into shared object transforms and implicit residuals via in-loop factorization, then trains a per-object ridge-conditioned language field from the resulting kinematic features. On HyperNeRF, the method achieves the highest reconstruction quality among all language-grounded and motion-aware methods (28.52 dB mean PSNR), closing to within 1.5 dB of unconstrained reconstruction-only systems while exposing interpretable motion primitives, temporally grounded language, and a structured scene export that no baseline provides. On targeted temporal-state retrieval, the kinematic-conditioned

field surpasses both LangSplat and 4D LangSplat by a wide margin (0.884 vs. 0.415 / 0.620 mean Acc, 0.815 vs. 0.304 / 0.433 mean vIoU, 0.733 vs. 0.262 / 0.439 mean tIoU), with the largest gains on motion-correlated state changes; ablation confirms that kinematic conditioning accounts for +0.45 tIoU over the static-embedding-only baseline.

References

- Jonathan T. Barron, Ben Mildenhall, Matthew Tancik, Peter Hedman, Ricardo Martin-Brualla, and Pratul P. Srinivasan. Mip-NeRF: A multiscale representation for anti-aliasing neural radiance fields. In *Proceedings of the IEEE/CVF International Conference on Computer Vision (ICCV)*, 2021.
- Rodney A Brooks. Symbolic reasoning among 3-d models and 2-d images. *Artificial Intelligence*, 17(1–3):285–348, 1981.
- Ang Cao and Justin Johnson. HexPlane: A fast representation for dynamic scenes. In *Proceedings of the IEEE/CVF Conference on Computer Vision and Pattern Recognition (CVPR)*, 2023.
- Susan Carey. *The Origin of Concepts*. Oxford University Press, New York, 2009.
- Nicolas Carion, Laura Gustafson, Yuan-Ting Hu, Shoubhik Debnath, Ronghang Hu, Didac Suris, Chaitanya Ryali, Kalyan Vasudev Alwala, Haitham Khedr, Andrew Huang, et al. Sam 3: Segment anything with concepts. *arXiv preprint arXiv:2511.16719*, 2025.
- Jiazhong Cen, Jiemin Fang, Chen Yang, Lingxi Xie, Xiaopeng Zhang, Wei Shen, and Qi Tian. Segment any 3D Gaussians. *arXiv preprint arXiv:2312.00860*, 2023.
- Jiazhong Cen, Jiemin Fang, Chen Yang, Lingxi Xie, Xiaopeng Zhang, Wei Shen, and Qi Tian. Segment anything in 3D with NeRFs. In *Advances in Neural Information Processing Systems (NeurIPS)*, 2023.
- Boyuan Chen, Max Simchowitz, and Vincent Sitzmann. Large video planner enables generalizable robot control. *arXiv preprint arXiv:2512.15840*, 2025.
- Mehdi Cherti, Romain Beaumont, Ross Wightman, Mitchell Wortsman, Gabriel Ilharco, Cade Gordon, Christoph Schuhmann, Ludwig Schmidt, and Jenia Jitsev. Reproducible scaling laws for contrastive language-image learning. In *Proceedings of the IEEE/CVF Conference on Computer Vision and Pattern Recognition (CVPR)*, 2023.
- Carl Doersch, Ankush Gupta, Larisa Markeeva, Adrià Recasens, Lucas Smaira, Yusuf Aytar, João Carreira, Andrew Zisserman, and Yi Yang. TAP-Vid: A benchmark for tracking any point in a video. In *Advances in Neural Information Processing Systems (NeurIPS)*, 2022.
- Carl Doersch, Yi Yang, Mel Veberčič, Relja Arandjelović, João Carreira, and Andrew Zisserman. TAPIR: Tracking any point with per-frame initialization and temporal refinement. In *Proceedings of the IEEE/CVF International Conference on Computer Vision (ICCV)*, 2023.
- Pedro F Felzenszwalb and Daniel P Huttenlocher. Pictorial structures for object recognition. *International Journal of Computer Vision*, 61(1):55–79, 2005.
- Gal Fiebelman, Tamir Cohen, Ayellet Morgenstern, Peter Hedman, and Hadar Averbuch-Elor. 4-LEGS: 4D language embedded gaussian splatting. *Computer Graphics Forum*, 2025.
- Sara Fridovich-Keil, Giacomo Meanti, Frederik Rahbæk Warburg, Benjamin Recht, and Angjoo Kanazawa. K-Planes: Explicit radiance fields in space, time, and

- appearance. In *Proceedings of the IEEE/CVF Conference on Computer Vision and Pattern Recognition (CVPR)*, 2023.
15. Chen Gao, Ayush Saraf, Johannes Kopf, and Jia-Bin Huang. Dynamic view synthesis from dynamic monocular video. In *Proceedings of the IEEE/CVF International Conference on Computer Vision (ICCV)*, 2021.
 16. Zhiyang Guo, Wengang Zhou, Li Li, Min Wang, and Houqiang Li. Motion-aware 3D Gaussian Splatting for efficient dynamic scene reconstruction. *arXiv preprint arXiv:2403.11447*, 2024.
 17. Danijar Hafner, Jurgis Pasukonis, Jimmy Ba, and Timothy Lillicrap. Mastering diverse domains through world models. *Nature*, 625:876–884, 2024.
 18. Richard Hartley and Andrew Zisserman. *Multiple View Geometry in Computer Vision*. Cambridge University Press, 2nd edition, 2003.
 19. Yi-Hua Huang, Yang-Tian Sun, Ziyi Yang, Xiaoyang Lyu, Yan-Pei Cao, and Xiaojuan Qi. SC-GS: Sparse-controlled gaussian splatting for editable dynamic scenes. In *Proceedings of the IEEE/CVF Conference on Computer Vision and Pattern Recognition (CVPR)*, 2024.
 20. Shengxiang Ji, Guanjun Wu, Jiemin Fang, Jiazhong Cen, Taoran Yi, Wenyu Liu, Qi Tian, and Xinggang Wang. Segment any 4D Gaussians. *arXiv preprint arXiv:2407.04504*, 2024.
 21. Nikita Karaev, Ignacio Rocco, Benjamin Graham, Natalia Neverova, Andrea Vedaldi, and Christian Rupprecht. CoTracker: It is better to track together. In *European Conference on Computer Vision (ECCV)*, 2024.
 22. Bernhard Kerbl, Georgios Kopanas, Thomas Leimkühler, and George Drettakis. 3D Gaussian Splatting for real-time radiance field rendering. *ACM Transactions on Graphics*, 42(4), 2023.
 23. Justin Kerr, Chung Min Kim, Ken Goldberg, Angjoo Kanazawa, and Matthew Tancik. LERF: Language embedded radiance fields. In *Proceedings of the IEEE/CVF International Conference on Computer Vision (ICCV)*, 2023.
 24. Alexander Kirillov, Eric Mintun, Nikhila Ravi, Hanzi Mao, Chloe Rolland, Laura Gustafson, Tete Xiao, Spencer Whitehead, Alexander C. Berg, Wan-Yen Lo, Piotr Dollár, and Ross Girshick. Segment anything. In *Proceedings of the IEEE/CVF International Conference on Computer Vision (ICCV)*, 2023.
 25. Alex Krizhevsky, Ilya Sutskever, and Geoffrey E Hinton. ImageNet classification with deep convolutional neural networks. In *Advances in Neural Information Processing Systems (NeurIPS)*, volume 25, 2012.
 26. Isaac Labe, Noam Issachar, Itai Lang, and Sagie Benaim. DGD: Dynamic 3D gaussians distillation. In *European Conference on Computer Vision*, pages 361–378. Springer, 2024.
 27. Junnan Li, Dongxu Li, Silvio Savarese, and Steven Hoi. BLIP-2: Bootstrapping language-image pre-training with frozen image encoders and large language models. In *International Conference on Machine Learning (ICML)*, 2023.
 28. Tianye Li, Mira Slavcheva, Michael Zollhöfer, Simon Green, Christoph Lassner, Changil Kim, Tanner Schmidt, Steven Lovegrove, Michael Goesele, Richard Newcombe, and Zhaoyang Lv. Neural 3D video synthesis from multi-view video. In *Proceedings of the IEEE/CVF Conference on Computer Vision and Pattern Recognition (CVPR)*, 2022.
 29. Wanhua Li, Renping Zhou, Jiawei Zhou, Yingwei Song, Johannes Herter, Minghan Qin, Gao Huang, and Hanspeter Pfister. 4D LangSplat: 4D language gaussian splatting via multimodal large language models. In *Proceedings of the IEEE/CVF Conference on Computer Vision and Pattern Recognition (CVPR)*, 2025.

30. Zhan Li, Zhang Chen, Zhong Li, and Yi Xu. Spacetime Gaussian feature splatting for real-time dynamic view synthesis. In *Proceedings of the IEEE/CVF Conference on Computer Vision and Pattern Recognition (CVPR)*, 2024.
31. Zhengqi Li, Simon Niklaus, Noah Snavely, and Oliver Wang. Neural scene flow fields for space-time view synthesis of dynamic scenes. In *Proceedings of the IEEE/CVF Conference on Computer Vision and Pattern Recognition (CVPR)*, 2021.
32. Youtian Lin, Zuozhuo Dai, Siyu Zhu, and Yao Yao. Gaussian-flow: 4d reconstruction with dynamic 3D gaussian particle. In *Proceedings of the IEEE/CVF Conference on Computer Vision and Pattern Recognition (CVPR)*, 2024.
33. Haotian Liu, Chunyuan Li, Qingyang Wu, and Yong Jae Lee. Visual instruction tuning. In *Advances in Neural Information Processing Systems (NeurIPS)*, 2023.
34. Yu-Lun Liu, Chen Gao, Andreas Meuleman, Hung-Yu Tseng, Ayush Saraf, Changil Kim, Yung-Yu Chuang, Johannes Kopf, and Jia-Bin Huang. Robust dynamic radiance fields. In *Proceedings of the IEEE/CVF Conference on Computer Vision and Pattern Recognition (CVPR)*, 2023.
35. David G Lowe. Distinctive image features from scale-invariant keypoints. *International Journal of Computer Vision*, 60(2):91–110, 2004.
36. Yiren Lu, Yunlai Zhou, Yiran Qiao, Chaoda Song, Tuo Liang, Jing Ma, and Yu Yin. Segment then splat: Unified 3D open-vocabulary segmentation via gaussian splatting. In *Advances in Neural Information Processing Systems (NeurIPS)*, 2024.
37. David Marr. *Vision: A Computational Investigation into the Human Representation and Processing of Visual Information*. W.H. Freeman, 1982.
38. Ben Mildenhall, Pratul P. Srinivasan, Matthew Tancik, Jonathan T. Barron, Ravi Ramamoorthi, and Ren Ng. NeRF: Representing scenes as neural radiance fields for view synthesis. In *European Conference on Computer Vision (ECCV)*, 2020.
39. Thomas Müller, Alex Evans, Christoph Schied, and Alexander Keller. Instant neural graphics primitives with a multiresolution hash encoding. *ACM Transactions on Graphics*, 41(4):1–15, 2022.
40. Keunhong Park, Utkarsh Sinha, Jonathan T. Barron, Sofien Bouaziz, Dan B. Goldman, Steven M. Seitz, and Ricardo Martin-Brualla. Nerfies: Deformable neural radiance fields. In *Proceedings of the IEEE/CVF International Conference on Computer Vision (ICCV)*, 2021.
41. Keunhong Park, Utkarsh Sinha, Peter Hedman, Jonathan T. Barron, Sofien Bouaziz, Dan B. Goldman, Ricardo Martin-Brualla, and Steven M. Seitz. HyperNeRF: A higher-dimensional representation for topologically varying neural radiance fields. *ACM Transactions on Graphics*, 40(6):1–12, 2021.
42. Albert Pumarola, Enric Corona, Gerard Pons-Moll, and Francesc Moreno-Noguer. D-NeRF: Neural radiance fields for dynamic scenes. In *Proceedings of the IEEE/CVF Conference on Computer Vision and Pattern Recognition (CVPR)*, 2021.
43. Minghan Qin, Wanhua Li, Jiawei Zhou, Haoqian Wang, and Hanspeter Pfister. LangSplat: 3D language gaussian splatting. In *Proceedings of the IEEE/CVF Conference on Computer Vision and Pattern Recognition (CVPR)*, 2024.
44. Alec Radford, Jong Wook Kim, Chris Hallacy, Aditya Ramesh, Gabriel Goh, Sandhini Agarwal, Girish Sastry, Amanda Askell, Pamela Mishkin, Jack Clark, Gretchen Krueger, and Ilya Sutskever. Learning transferable visual models from natural language supervision. In *International Conference on Machine Learning (ICML)*, 2021.

45. Nikhila Ravi, Valentin Gabeur, Yuan-Ting Hu, Ronghang Hu, Chaitanya Ryali, Tengyu Ma, Haitham Khedr, Roman Rädle, Chloe Rolland, Laura Gustafson, Eric Mintun, Junting Pan, Kalyan Vasudev Alwala, Nicolas Carion, Chao-Yuan Wu, Ross Girshick, Piotr Dollár, and Christoph Feichtenhofer. SAM 2: Segment anything in images and videos. *arXiv preprint arXiv:2408.00714*, 2024.
46. Johannes L. Schönberger and Jan-Michael Frahm. Structure-from-motion revisited. In *Proceedings of the IEEE/CVF Conference on Computer Vision and Pattern Recognition (CVPR)*, 2016.
47. Jin-Chuan Shi, Miao Wang, Hao-Bin Duan, and Shao-Hua Guan. Language embedded 3D Gaussians for open-vocabulary scene understanding. In *Proceedings of the IEEE/CVF Conference on Computer Vision and Pattern Recognition (CVPR)*, 2024.
48. Vincent Sitzmann. The flavor of the bitter lesson for computer vision. https://www.vincent Sitzmann.com/blog/bitter_lesson_of_cv/, 2026.
49. Linda Smith and Michael Gasser. The development of embodied cognition: Six lessons from babies. *Artificial Life*, 11(1–2):13–29, 2005.
50. Linda B. Smith, Swapnaa Jayaraman, Elizabeth Clerkin, and Chen Yu. The developing infant creates a curriculum for statistical learning. *Trends in Cognitive Sciences*, 22(4):325–336, 2018.
51. Kiwhan Song, Boyuan Chen, Max Simchowitz, Yilun Du, Russ Tedrake, and Vincent Sitzmann. History-guided video diffusion. *arXiv preprint arXiv:2502.06764*, 2025.
52. Elizabeth S. Spelke. Principles of object perception. *Cognitive Science*, 14(1):29–56, 1990.
53. Elizabeth S Spelke. Core knowledge. *American Psychologist*, 55(11):1233–1243, 2000.
54. Richard S. Sutton. The bitter lesson. <https://www.incompleteideas.net/IncIdeas/BitterLesson.html>, 2019.
55. Jianyuan Wang, Nikita Karaev, Christian Rupprecht, and David Novotny. VG-GSfM: Visual geometry grounded deep structure from motion. In *Proceedings of the IEEE/CVF Conference on Computer Vision and Pattern Recognition (CVPR)*, 2024.
56. Sandra R. Waxman and Dana B. Markow. Words as invitations to form categories: Evidence from 12- to 13-month-old infants. *Cognitive Psychology*, 29(3):257–302, 1995.
57. Guanjun Wu, Taoran Yi, Jiemin Fang, Lingxi Xie, Xiaopeng Zhang, Wei Wei, Wenyu Liu, Qi Tian, and Xinggang Wang. 4D Gaussian Splatting for real-time dynamic scene rendering. In *Proceedings of the IEEE/CVF Conference on Computer Vision and Pattern Recognition (CVPR)*, 2024.
58. Ziyi Yang, Xinyu Gao, Wen Zhou, Shaohui Jiao, Yuqing Zhang, and Xiaogang Jin. Deformable 3D Gaussians for high-fidelity monocular dynamic scene reconstruction. In *Proceedings of the IEEE/CVF Conference on Computer Vision and Pattern Recognition (CVPR)*, 2024.
59. Mingqiao Ye, Martin Danelljan, Fisher Yu, and Lei Ke. Gaussian grouping: Segment and edit anything in 3D scenes. In *European Conference on Computer Vision (ECCV)*, 2024.
60. Xiaohua Zhai, Basil Mustafa, Alexander Kolesnikov, and Lucas Beyer. Sigmoid loss for language image pre-training. In *Proceedings of the IEEE/CVF International Conference on Computer Vision (ICCV)*, 2023.

61. Richard Zhang, Phillip Isola, Alexei A Efros, Eli Shechtman, and Oliver Wang. The unreasonable effectiveness of deep features as a perceptual metric. In *Proceedings of the IEEE/CVF Conference on Computer Vision and Pattern Recognition (CVPR)*, 2018.
62. Shijie Zhou, Haoran Chang, Sicheng Jiang, Zhiwen Fan, Zehao Zhu, Dejie Xu, Pradyumna Chari, Suyu You, Zhangyang Wang, and Achuta Kadambi. Feature 3DGS: Supercharging 3D Gaussian Splatting to enable distilled feature fields. In *Proceedings of the IEEE/CVF Conference on Computer Vision and Pattern Recognition (CVPR)*, 2024.

Supplementary Material

4D Synchronized Fields: Motion-Language Gaussian Splatting for Temporal Scene Understanding

Reconstruction

Language grounding

Motion structure

Synchronized (ours)

This supplementary uses the same color code as the main paper. Appendix A: architecture, hyperparameters, training. Appendix B: kinematic features. Appendix C: diagnostics. Appendices D–F: definitions, notation, evaluation. Appendix G: discussion and design concerns. Appendix H: baselines. Appendix I: failure cases. Appendix J: broader impact.

A Architecture and Implementation

A.1 Deformation MLP \mathcal{D}_θ

Input: $[\mathbf{x}_i^0; \mathbf{z}_i; \gamma(t)] \in \mathbb{R}^{48}$ (3+32+13). Architecture (4 layers, hidden 128):

$$\begin{aligned} \text{Lin}(48, 128) &\rightarrow \text{ReLU} \rightarrow \text{Lin}(128, 128) \rightarrow \text{ReLU} \rightarrow \\ &\text{Lin}(128, 128) \rightarrow \text{ReLU} \rightarrow \text{Lin}(128, 9). \end{aligned}$$

Final layer zero-initialized (identity deformation at start). Output scaled: $\Delta \mathbf{x} = 0.10 \cdot \mathbf{o}_{0:3}$, $\Delta \boldsymbol{\omega} = 0.10 \cdot \mathbf{o}_{3:6}$, $\Delta \boldsymbol{\ell} = 0.05 \cdot \mathbf{o}_{6:9}$. Total: $\sim 0.13\text{M}$ parameters.

Sinusoidal encoding ($L = 6$ bands):

$$\begin{aligned} \gamma(t) = [t, \sin(2^0 \pi t), \cos(2^0 \pi t), \dots, \\ \sin(2^5 \pi t), \cos(2^5 \pi t)]^\top. \end{aligned}$$

A.2 Object Motion Model \mathcal{M}_ϕ

Per-frame (default). Parameters: $\boldsymbol{\omega}_k \in \mathbb{R}^{K \times T \times 3}$ (rotation vectors), $\mathbf{t}_k \in \mathbb{R}^{K \times T \times 3}$ (translations). Init: $\mathcal{N}(0, 10^{-8})$. Smoothness via finite differences:

$$\begin{aligned} \mathcal{L}_{\text{smooth}} = \frac{1}{K} \sum_k (\|\boldsymbol{\omega}_k[t] - \boldsymbol{\omega}_k[t-1]\|^2 \\ + \|\mathbf{t}_k[t] - \mathbf{t}_k[t-1]\|^2). \end{aligned}$$

Identity prior on static objects: $\lambda_{\text{id}} = 0.001$. LR cosine-annealed $10^{-3} \rightarrow 10^{-5}$.

MLP variant (implemented, not used). Input: per-object embedding $\mathbf{e}_k^{\text{obj}} \in \mathbb{R}^{16}$ concatenated with $\gamma(t)$. 3-layer MLP, hidden 64, zero-init output, outputs 6 (SE3) or 12 (affine).

Affine variant. $\Delta \mathbf{A}_k \in \mathbb{R}^{K \times T \times 3 \times 3}$ (affine delta), $\mathbf{b}_k \in \mathbb{R}^{K \times T \times 3}$ (bias). Transform: $\tilde{\mathbf{x}}_i = (\mathbf{I} + \Delta \mathbf{A}_{o(i)}) \mathbf{x}_i^0 + \mathbf{b}_{o(i)}$.

A.3 Gaussian Scene Initialization

From COLMAP: $\mathbf{q}_i^0 = [1, 0, 0, 0]$, $\mathbf{s}_i^0 = \log(0.02)$, $\alpha_i^{\text{logit}} = \text{logit}(0.1)$, SH DC band from point colors, $\mathbf{z}_i \sim \mathcal{N}(0, 0.01^2)$. Quaternion convention: (w, x, y, z) throughout. Axis-angle to quaternion:

$$\begin{aligned} \text{aa2q}(\boldsymbol{\omega}) &= \text{normalize} \left[\cos(\theta/2), \right. \\ &\quad \left. (\boldsymbol{\omega}/(\theta+\varepsilon)) \sin(\theta/2) \right], \\ \theta &= \|\boldsymbol{\omega}\|, \quad \varepsilon = 10^{-8}. \end{aligned}$$

A.4 Residual-Adaptive Modulation

EMA update: $\bar{r}_i \leftarrow 0.95 \bar{r}_i + 0.05 \|\mathbf{r}_i(t)\|_2$. Weight: $m_i = \sigma((\bar{r}_i - \mu_{\bar{r}})/(\sigma_{\bar{r}} + 10^{-6}))$. Re-initialized when densification changes N .

A.5 Photometric Loss

$\mathcal{L}_{\text{rgb}} = 0.8 \|\hat{\mathbf{F}} - \mathbf{F}\|_1 + 0.2 \text{DSSIM}(\hat{\mathbf{F}}, \mathbf{F})$, where $\text{DSSIM} = (1 - \text{SSIM})/2$ via 3×3 average-pool SSIM.

A.6 Hyperparameters

All values fixed across all six HyperNeRF scenes.

\mathcal{D}_θ : hidden 128, 4 layers, $D_z=32$, $L=6$, output scales 0.10/0.10/0.05.

Photometric: $\lambda_1=0.8$, $\lambda_{\text{dssim}}=0.2$.

Densification: grad thresh 2×10^{-4} , range 500–15k, interval 100, max $N=10^6$.

\mathcal{M}_ϕ : per-frame SE(3), init $\sigma=10^{-4}$.

Regularizers: $\lambda_{\text{res}}=0.02$, $\lambda_{\text{share}}=0.01$, $\tau=0.35$, $\lambda_{\text{vel}}=0.01$, $\lambda_{\text{smooth}}=0.01$, $\lambda_{\text{id}}=0.001$, $\eta=0.95$.

Staged activation (Phase 2): \mathcal{M}_ϕ start 200, vel. start 300, warmup 500–1000, residual start 600, ramp 800.

Language field: SigLIP-base-patch16-224, ridge $\lambda=0.01$, blend $\beta=0.65$, temporal EMA $\gamma=0.15$, query weights $w_s=0.35$ / $w_t=0.65$.

Assignment: min votes 3, min consistency 0.6.

Optimization: LR scene/deform 5×10^{-4} , LR \mathcal{M}_ϕ : $10^{-3} \rightarrow 10^{-5}$ (cosine), Phase 1: 30k iter, Phase 2: 20k iter, seed 42.

A.7 Training Procedure

■ **Phase 1 (~29 min, A100)**. Standard deformable 4DGS: \mathcal{L}_{rgb} + densification. No motion decomposition.

■ **Phase 2 (~12 min)**. From Phase 1 checkpoint. Introduces \mathcal{M}_ϕ with staged loss activation: iter ≥ 200 : $\mathcal{L}_{\text{smooth}}, \mathcal{L}_{\text{share}}, \mathcal{L}_{\text{id}}$; iter ≥ 300 : $+\mathcal{L}_{\text{vel}}$; iter 500–1000: linear warmup (0%→100%) of all auxiliary losses; iter ≥ 600 : $+\mathcal{L}_{\text{res}}^{\text{mod}}$ with modulation EMA; iter ≥ 1000 : full weights.

Simultaneous activation at iter 0 causes $\bar{\rho}$ to plateau below 0.15 because \mathcal{D}_θ absorbs all motion before \mathcal{M}_ϕ converges. The 400-iteration head start lets shared transforms capture the dominant rigid component first.

■ **Phase 3 (<1 min)**. On frozen Phase 2 checkpoint: (1) project objects into frames, extract bounding-box crops (2nd–98th percentile, 12% margin); (2) encode via SigLIP: $\mathbf{e}_{k,f}^{\text{obs}} \in \mathbb{R}^{768}$; (3) static embeddings: $\mathbf{e}_k^{\text{static}} = \text{norm}(\text{mean}_f \mathbf{e}_{k,f}^{\text{obs}})$; (4) extract 28D kinematics (§B); (5) per-object ridge fit (closed-form); (6) blend ($\beta = 0.65$) + temporal EMA ($\gamma = 0.15$).

B 28D Kinematic Feature Vector

■ Constructed per object-time pair (k, f) from the frozen Phase 2 checkpoint.

■ **Core motion (dims 0–5)**: 0: speed $\|\mathbf{v}_k(f)\|$; 1: acceleration magnitude $\|\mathbf{a}_k(f)\|$; 2: angular velocity from consecutive $\boldsymbol{\omega}_k$ of \mathcal{M}_ϕ ; 3: residual mean $|\mathcal{S}_k|^{-1} \sum_{i \in \mathcal{S}_k} \|\mathbf{r}_i\|$; 4: per-object rigid share $\rho_k(f)$; 5: visibility fraction of \mathcal{S}_k .

■ **Directional + temporal derivatives (dims 6–15)**: 6–8: velocity (v_x, v_y, v_z) ; 9–11: acceleration (a_x, a_y, a_z) ; 12: speed delta $s_k(f) - s_k(f-1)$; 13: rigid-share delta $\rho_k(f) - \rho_k(f-1)$; 14: EMA-smoothed speed (decay ≈ 5 frames); 15: EMA-smoothed acceleration magnitude.

■ **Transform diagnostics (dims 16–19)**: 16: rotation angle $\|\boldsymbol{\omega}_k(f)\|$ from \mathcal{M}_ϕ ; 17: translation magnitude $\|\mathbf{t}_k(f)\|$; 18: residual std $\text{std}_{i \in \mathcal{S}_k} \|\mathbf{r}_i(f)\|$; 19: affine delta Frobenius norm $\|\Delta \mathbf{A}_k(f)\|_F$ (zero in SE3 mode).

■ **Relational context (dims 20–27)**: 20: relative speed s_k/s_{ref} (95th-pct scene speed); 21: fractional speed rank among objects at f ; 22: binary is-fastest indicator; 23: time fraction $f/(T-1)$; 24: min centroid distance to other objects; 25: closing speed to nearest (d/dt of dim 24; negative = approach); 26: distance to hand object; 27: closing speed to hand (d/dt of dim 26).

Standardization. Per-object: $\tilde{f}_{k,f}^{(d)} = (f_{k,f}^{(d)} - \mu_k^{(d)})/(\sigma_k^{(d)} + 10^{-8})$, statistics over \mathcal{F}_k . Bias appended $\rightarrow \tilde{\mathbf{f}}_{k,f} \in \mathbb{R}^{29}$.

C Object Assignment and Diagnostics

C.1 Object Assignment

■ Masks from SAM 3 (indexed PNGs or per-object binary folders; any segmenter substitutes). For each training frame, all Gaussians are projected; each landing on label > 0 adds one vote. Assignment: $o(i) = \arg \max_{k \geq 1} \mathbf{V}[i, k]$,

subject to $\sum_{k \geq 1} \mathbf{V}[i, k] \geq 3$ and $\mathbf{V}[i, o(i)] / \sum_{k \geq 1} \mathbf{V}[i, k] \geq 0.6$. Failures \rightarrow background. Objects with fewer than a configurable minimum count are merged to background.

Per-scene K (incl. background): americano 5, chickchicken 4, espresso 5, keyboard 7, split-cookie 4, torchocolate 6.

C.2 Diagnostics and Shuffle Test

■ Residual mean.

$$\begin{aligned}\bar{r}_k &= |\mathcal{F}_k|^{-1} \sum_f \hat{r}_k(f), \\ \hat{r}_k(f) &= |\mathcal{S}_k|^{-1} \sum_{i \in \mathcal{S}_k} \|\mathbf{r}_i(f)\|.\end{aligned}$$

Per-object motion variance.

$$V_k(f) = |\mathcal{S}_k|^{-1} \sum_{i \in \mathcal{S}_k} \left\| (\mathbf{x}_i(f) - \mathbf{x}_i^0) - \overline{\Delta \mathbf{x}_k}(f) \right\|^2.$$

Shuffle test. Evaluate with correct assignments ($\bar{\rho}$, \bar{r}); generate 5 random permutations; re-evaluate *without retraining*. Result: permuted labels increase residual energy by 1.52 \times , confirming object-specificity.

Per-scene rigid share. americano 0.508 (res. 0.032, rigid pouring); chickchicken 0.451 (0.041, mixed); espresso 0.411 (0.045, fluid/non-rigid); keyboard 0.422 (0.043, articulated); split-cookie 0.528 (0.029, two rigid pieces); torchocolate 0.478 (0.035, rigid manipulation). The one-sided hinge ($\tau = 0.35$) imposes zero penalty on scenes exceeding the target.

D Definitions and Terminology

Canonical frame. Reference frame for Gaussian parameters ($\mathbf{x}_i^0, \mathbf{q}_i^0, \mathbf{s}_i^0$); deformations are displacements from this frame.

■ **In-loop.** Computation whose gradients affect scene/deformation parameters during reconstruction (contrast: post-hoc distillation).

■ **Implicit residual.** $\mathbf{r}_i(t) = \mathbf{x}_i(t) - \tilde{\mathbf{x}}_i(t)$: derived analytically from $\mathcal{D}_\theta / \mathcal{M}_\phi$; enters optimization only through regularizers.

■ **Residual-adaptive modulation.** Tracks per-Gaussian residual via EMA; reduces penalty for persistently high-residual Gaussians (boundaries, articulated regions).

■ **Rigid-share hinge.** One-sided loss on $\rho(t)$: active only when $\rho < \tau$; scenes exceeding τ incur zero penalty.

■ **Synchronized.** Language field conditioned on kinematic features from \mathcal{M}_ϕ , not post-hoc distillation onto a frozen backbone.

■ **Ridge map.** Per-object closed-form regression: $\mathbf{W}_k = (\tilde{\mathbf{F}}_k^\top \tilde{\mathbf{F}}_k + \lambda \mathbf{I})^{-1} \tilde{\mathbf{F}}_k^\top \Delta \mathbf{E}_k$.

■ **Semantic residual.** $\Delta \mathbf{e}_{k,f} = \mathbf{e}_{k,f}^{\text{obs}} - \mathbf{e}_k^{\text{static}}$: time-varying deviation from temporal mean.

E Notation Reference

■ *Scene and Gaussians.* N : total Gaussians; K : objects (incl. background at 0); T : training frames. $\mathbf{x}_i^0 \in \mathbb{R}^3$, $\mathbf{q}_i^0 \in \mathbb{S}^3$, $\mathbf{s}_i^0 \in \mathbb{R}^3$: canonical position, quaternion (w, x, y, z) , log-scale. $\mathbf{c}_i \in \mathbb{R}^{16 \times 3}$: SH coefficients (degree $d = 3$). $\mathbf{z}_i \in \mathbb{R}^{32}$: per-Gaussian deformation embedding. $o(i) \in \{0 \dots K-1\}$: object assignment; \mathcal{S}_k : Gaussian index set for object k ; \mathcal{F}_k : visible-frame set.

■ *Deformation.* \mathcal{D}_θ : deformation MLP. $\gamma(t) \in \mathbb{R}^{13}$: sinusoidal time encoding ($L = 6$ bands + raw input). $\Delta \mathbf{x}_i, \Delta \boldsymbol{\omega}_i, \Delta \boldsymbol{\ell}_i \in \mathbb{R}^3$: position, axis-angle rotation, log-scale deltas.

■ *Object motion.* \mathcal{M}_ϕ : object motion model. $\boldsymbol{\omega}_k(t), \mathbf{t}_k(t) \in \mathbb{R}^3$: per-object rotation vector, translation. $\mathbf{R}_k(t) \in \text{SO}(3)$: rotation matrix from $\boldsymbol{\omega}_k(t)$. $\tilde{\mathbf{x}}_i(t) \in \mathbb{R}^3$: object-predicted position. $\mathbf{r}_i(t) \in \mathbb{R}^3$: implicit residual. $\rho(t) \in [0, 1]$: rigid-share ratio. $m_i \in [0, 1]$: modulation weight. $\tilde{r}_i \in \mathbb{R}_+$: EMA-tracked residual magnitude.

■ *Language field.* $E_{\text{img}}/E_{\text{txt}}$: SigLIP image/text encoder; $D_e = 768$. $\mathbf{e}_{k,f}^{\text{obs}}, \mathbf{e}_k^{\text{static}}, \mathbf{e}_{k,f}^{\text{sync}} \in \mathbb{R}^{D_e}$: observation, static, synchronized embeddings. $\mathbf{f}_{k,f} \in \mathbb{R}^{28}$: kinematic feature vector; $\tilde{\mathbf{f}}_{k,f} \in \mathbb{R}^{29}$: standardized + bias. $\mathbf{W}_k \in \mathbb{R}^{29 \times D_e}$: ridge weight matrix.

■ *Losses.* \mathcal{L}_{rgb} : photometric (L1+DSSIM). $\mathcal{L}_{\text{res}}^{\text{mod}}$: modulated residual energy. $\mathcal{L}_{\text{share}}$: rigid-share hinge ($\tau = 0.35$). \mathcal{L}_{vel} : velocity coherence. $\mathcal{L}_{\text{smooth}}$: temporal smoothness on \mathcal{M}_ϕ . $\eta = 0.95$: modulation EMA decay.

F Evaluation Protocol

■ **Task.** Given query q and GT interval $[f_s, f_e]$, produce binary per-frame activation.

Thresholding (all methods).

$$\text{active}(f) = \mathbb{1}[\langle \mathbf{e}_{k,f}^{\text{sync}}, \mathbf{e}_q \rangle > 0.5 \cdot \max_{f'} \langle \mathbf{e}_{k,f'}^{\text{sync}}, \mathbf{e}_q \rangle].$$

The threshold (50% of peak similarity) is applied identically to all methods. For baselines that produce per-pixel rather than per-object embeddings, we aggregate by averaging within the GT object mask.

Metric definitions.

Acc (frame-level binary accuracy): fraction of frames where the binary activation matches the GT label. $\text{Acc} = T^{-1} \sum_f \mathbb{1}[\text{active}(f) = \text{gt}(f)]$.

vIoU (volumetric IoU): spatial mask IoU computed per active frame, then averaged over the union of predicted and GT active frames. This follows the 4D LangSplat evaluation code; we use their released evaluation script without modification.

tIoU (temporal interval IoU): $|P \cap G| / |P \cup G|$, where P and G are the sets of predicted-active and GT-active frame indices, respectively. This metric is agnostic to spatial mask quality and isolates temporal precision.

Query-to-state mapping. Each evaluation scene has human-annotated per-frame state labels (e.g., americano: “pre-pour”, “pouring”, “luminous-liquid”, “settling”; espresso: “empty”, “filling”, “above-midpoint”, “full”). For each state, we define a natural-language query that a user might issue (e.g., “glass in luminous-liquid phase”, “glass cup with liquid above midpoint”). The GT temporal interval is the contiguous frame range where that state label is active. Queries are designed to require temporal reasoning: the object identity is constant across the sequence, so only the temporal component of the scoring function (Eq. 15 of the main paper) can distinguish when the state holds.

Reconciliation with 4D LangSplat metrics. Both our evaluation and 4D LangSplat’s use Acc and vIoU, computed on the same HyperNeRF scenes at matched $2\times$ resolution with shared held-out frames. We use 4D LangSplat’s official evaluation code and test split. The apparent discrepancy between the 4D LangSplat numbers in our Table 2 of the main paper and those in the 4D LangSplat paper arises because 4D LangSplat’s paper reports results on object-identity queries (“find the cup”), where temporal precision is irrelevant, while our evaluation targets temporal-state queries (“find the cup *while being filled*”), which require distinguishing *when* a state holds. On identity queries, 4D LangSplat performs well because its MLLM-supervised dual semantic field captures *what* is present; on state queries, it underperforms because it lacks structured access to *how* and *when* objects move, which is exactly what kinematic conditioning provides.

Annotations. Per-frame state labels and query-to-state mappings were obtained from the 4D LangSplat evaluation repository. Each scene has human-annotated temporal intervals marking when each state holds (e.g., “luminous-liquid phase” for americano, “liquid above midpoint” for espresso). We use these annotations without modification. The 50% peak-similarity threshold was fixed globally and not tuned per scene or per query.

G Dataset and Baselines

HyperNeRF. 6 scenes, $2\times$ resolution (4D LangSplat test split), RGB scale factor 8, shared COLMAP initialization and held-out frames.

Baselines.

Language-grounded 4D LangSplat (official code, CLIP+MLLM captions), LangSplat (static 3D), LERF, LEGaussians.

Reconstruction-only Deformable-3DGS, SC-GS, 4DGaussians, 3DGS.

Motion-aware MotionGS.

4-LEGS and DGD discussed in §2 but excluded (no public code on HyperNeRF).

H Discussion and Addressing Concerns

H.1 \mathcal{M}_ϕ Architecture: Table vs. Function

■ The default \mathcal{M}_ϕ stores per-object per-frame SE(3) parameters as a $K \times T \times 6$ tensor. Chosen because it (i) avoids a second temporal MLP whose capacity must be balanced against \mathcal{D}_θ , (ii) provides direct gradient flow from regularizers to each frame’s parameters, which is critical for staged activation (§A.7), and (iii) admits explicit temporal smoothness via $\mathcal{L}_{\text{smooth}}$. For $K = 5$, $T = 150$: 4,500 floats (<0.01M), negligible relative to \mathcal{D}_θ ($\sim 0.13\text{M}$).

The table does not interpolate to unseen timesteps. An MLP variant (3-layer, hidden 64, zero-initialized output, learnable object embeddings $\in \mathbb{R}^{K \times 16}$) is implemented but not used in reported experiments: it adds hyperparameter sensitivity without improving within-sequence metrics. The temporal smoothness regularizer $\mathcal{L}_{\text{smooth}}$ acts as an implicit continuous-time prior on the discrete table: penalizing frame-to-frame differences is equivalent to a first-order finite-difference smoothness prior, which for densely sampled sequences approximates a continuous smoothness constraint.

H.2 Renderer-Unchanged Property

■ A key design principle is that the forward rendering path is *never modified*: $\mathbf{x}_i(t)$ produced by \mathcal{D}_θ is rendered directly via standard alpha-compositing. The decomposition $\mathbf{x}_i(t) = \tilde{\mathbf{x}}_i(t) + \mathbf{r}_i(t)$ injects signal only through regularizers; removing \mathcal{M}_ϕ entirely recovers exact baseline rendering. This property provides three guarantees: (i) reconstruction quality can only improve or remain neutral relative to the backbone (confirmed by the +0.07 dB in the w/o \mathcal{M}_ϕ ablation, Table 3 of the main paper); (ii) compatibility with any Gaussian splatting renderer (CUDA, software, hardware); (iii) the decomposition is a pure inductive bias: it shapes what is learned, not how it is rendered. To our knowledge, this renderer-unchanged property has not been explicitly demonstrated in prior language-grounded or motion-aware dynamic Gaussian methods.

H.3 Identifiability of the Decomposition

■ The decomposition is not formally identifiable: without regularizers, \mathcal{D}_θ absorbs all motion into residuals. The five regularizers break this degeneracy by imposing a preference for shared motion. Three lines of evidence confirm the decomposition is non-trivial and stable:

(i) The shuffle test (§C.2) shows $1.52\times$ residual energy increase under permuted assignments, confirming object-specificity.

(ii) Per-scene rigid-share ratios vary consistently with physical content: split-cookie (two rigid pieces, $\bar{\rho} = 0.528$) > americano (rigid pouring, 0.508) > chickchicken (mixed, 0.451) > keyboard (articulated, 0.422) > espresso (fluid, 0.411). This ordering would not emerge from a degenerate factorization.

(iii) Hyperparameters are fixed across all six scenes. The one-sided hinge ($\tau = 0.35$) self-regulates: scenes naturally exceeding τ incur zero penalty. Simultaneous loss activation (ablation, §4.4) collapses $\bar{\rho}$ below 0.15; the staged schedule prevents this by giving \mathcal{M}_ϕ a head start before residual regularization activates.

H.4 Hyperparameter Design Rationale

■ The regularizer weights $\lambda_{\text{res}} = 0.02$, $\lambda_{\text{share}} = 0.01$, $\lambda_{\text{vel}} = 0.01$, $\lambda_{\text{smooth}} = 0.01$ are set once and used across all scenes without per-scene tuning. The key stabilizing factor is the one-sided hinge on ρ : it imposes a *floor* ($\tau = 0.35$) on the rigid-share ratio without imposing a ceiling. Scenes with naturally high rigidity (split-cookie: $\rho = 0.528$) exceed τ and receive zero hinge penalty; scenes with substantial non-rigid motion (espresso: $\rho = 0.411$) hover near τ and receive gentle pressure. This asymmetric design is why fixed hyperparameters work across scenes with very different motion characteristics.

The residual-adaptive modulation further reduces sensitivity: Gaussians with persistently high residuals (23% of all Gaussians, concentrated on boundaries and articulated regions) are automatically down-weighted, preventing the residual penalty from fighting genuinely non-rigid motion. Together, the hinge and modulation create a self-regulating system that adapts to per-scene motion complexity without requiring manual tuning.

H.5 Assignment Robustness

■ Multiview voting (≥ 3 votes, $\geq 60\%$ consistency) suppresses per-frame segmentation noise. If the segmenter produces inconsistent IDs across frames, SAM 3’s video propagation mitigates this; residual cases resolve to the plurality label or fall to background (reducing coverage, not introducing incorrect constraints).

The assignment is a pre-processing step: changing the segmenter changes only the input to \mathcal{M}_ϕ , not the architecture or training procedure. This modularity means the method inherits whatever robustness the segmenter provides, and benefits from future segmentation improvements without modification.

Unsupervised assignment (clustering coherent deformation trajectories from D_θ) is viable; only the assignment stage changes. Not pursued because the contribution is synchronization, not segmentation.

H.6 Occlusion Handling in the Language Field

■ Three mechanisms handle missing observations:

(i) **Kinematic prediction.** When object k is not visible in frame f (no crop available), the ridge-map prediction $\hat{\mathbf{e}}_{k,f} = \text{norm}(\mathbf{e}_k^{\text{static}} + \tilde{\mathbf{f}}_{k,f}^\top \mathbf{W}_k)$ is used as the sole embedding. Since kinematic features (centroid position, velocity, rigid share) are available for all assigned Gaussians regardless of camera visibility, the prediction is well-defined even under full occlusion.

(ii) **Temporal EMA.** A smoothing pass ($\gamma = 0.15$) propagates information from neighboring observed frames into occluded intervals, preventing abrupt embedding discontinuities at occlusion boundaries.

(iii) **Graceful degradation.** Under prolonged occlusion where kinematic features are also uninformative (e.g., a stationary occluded object), the predicted embedding converges to $\mathbf{e}_k^{\text{static}}$, i.e. the object’s time-averaged identity. This is the correct fallback: without motion or visual evidence, the best estimate is the static anchor. The system never produces undefined or missing embeddings.

H.7 Why Linear Ridge Regression

Chosen for (i) closed-form solution (no gradient-based training, no learning rate, no convergence issues), (ii) inability to overfit small per-object sample counts ($|\mathcal{F}_k| \approx 50\text{--}200$), and (iii) fully staged training with no gradient coupling between SigLIP and the photometric loss.

The closed-form property is particularly important: it means the language field adds exactly zero training instability to the system. The entire Phase 3 is deterministic given the Phase 2 checkpoint.

The +0.45 tIoU gain over static-only (Table 5 of the main paper) confirms substantial temporal signal captured linearly. Narrower chickchicken gain (+0.31) suggests nonlinearity may help for appearance-driven states. However, the linear map already more than doubles the temporal localization quality of 4D LangSplat (0.733 vs. 0.439 tIoU), indicating that the bottleneck is not model capacity but the quality of kinematic features, which is exactly what the in-loop factorization provides.

H.8 Why SigLIP

SigLIP’s sigmoid contrastive loss produces per-pair calibrated similarities, unlike CLIP/OpenCLIP’s softmax (batch-relative probabilities). Critical for Eq. 15’s cross-object scoring, where absolute magnitudes are compared across objects and timesteps without a fixed candidate set. This calibration property is orthogonal to model capacity: it ensures that a score of 0.7 for object A and 0.6 for object B reflects a genuine difference in match quality, rather than an artifact of the normalization denominator.

H.9 Fairness vs. 4D LangSplat

4D LangSplat uses CLIP + MLLM captions (richer semantic supervision); we use SigLIP only (no MLLM). Despite this supervision asymmetry, 4D SYNCHRONIZED FIELDS leads on all temporal-state metrics (Table 2 of the main paper) and reconstruction (Table 1 of the main paper). This indicates that for motion-correlated state changes, kinematic conditioning provides a stronger signal than additional language supervision alone.

H.10 Motion Factorization Evaluation

■ No existing benchmark provides GT per-object SE(3) for real monocular video. We rely on four internal diagnostics (§C): residual mean, rigid-share ratio, shuffle test, per-object motion variance. Physical consistency of $\bar{\rho}$ across scenes (higher for rigid scenes (split-cookie: 0.528), lower for deformable ones (espresso: 0.411)) suggests the factorization reflects scene content.

Critically, the motion factorization is not an end in itself but a means to language synchronization. The temporal-state retrieval results (Table 2 of the main paper) serve as an *extrinsic* evaluation of motion quality: if the SE(3) factors were incorrect, the kinematic features derived from them would not improve temporal localization. The +0.45 tIoU gain from kinematic conditioning (Table 5 of the main paper) therefore constitutes indirect but strong evidence that the learned motion structure is semantically meaningful.

H.11 Relationship to DynMF

■ DynMF factorizes motion globally via time-only basis trajectories with per-Gaussian coefficients, with no object identity, no language coupling, no physical interpretation of the bases. Three structural differences: (i) DynMF’s bases are shared across all points; ours are per-object, enabling object-level kinematic feature extraction. (ii) DynMF’s bases lack physical semantics (rotation, translation); our SE(3) parameters have direct rigid-body interpretation. (iii) DynMF does not condition any downstream task on its factorization; we condition language on kinematics. The approaches are complementary: DynMF’s low-rank structure could serve as an alternative backbone, with our per-object SE(3) layer and language field applied on top.

H.12 Relationship to CIF

■ CIF trains an explicit instance field for panoptic segmentation with deformable Gaussians. Key differences: (i) CIF’s instance field targets segmentation, not motion decomposition; it does not produce per-object SE(3) factors or kinematic features. (ii) CIF’s semantics are class-level (panoptic labels), not open-vocabulary temporal embeddings. (iii) CIF does not expose a kinematic-conditioned language field for temporal queries. Complementary: CIF’s learned instance field could replace our SAM-based assignment, providing end-to-end instance consistency. No public code on HyperNeRF at submission time precluded empirical comparison.

H.13 Relationship to 4DGS Variants and Streaming Methods

■ Native 4D Gaussian primitives (4DGS, Hybrid 3D-4DGS) model dynamics by extending Gaussians with temporal extent, offering efficiency gains for reconstruction. Their goals differ from ours (no language, no object factorization),

but they could serve as alternative backbones: our decomposition operates on deformed positions $\mathbf{x}_i(t)$ regardless of how they are produced.

Streaming/online methods (FLAG-4D, DASS) target temporal coherence via flow cues or online adaptation. Our synchronization could integrate with such pipelines by applying the motion decomposition and language field to incrementally updated Gaussian sets, though this would require adapting the per-frame \mathcal{M}_ϕ table to a growing sequence.

H.14 Scalability with K

■ K ranges 3–7 in our experiments. \mathcal{M}_ϕ cost scales linearly: one transform retrieval per object per forward pass. Memory for $K = 20$, $T = 300$: 36K floats (≈ 140 KB). No instabilities for $K \leq 10$. The ridge fit is independent per object: adding objects increases computation linearly with no cross-object coupling.

H.15 Generality Beyond Curated Queries

■ The evaluation in Table 2 of the main paper uses curated query-state mappings to enable precise quantitative measurement. However, the language field supports *arbitrary* open-vocabulary queries via the scoring function (Eq. 15): any text string encoded by SigLIP can be scored against all object-time embeddings. The restriction to curated queries is an evaluation choice, not a method limitation. The static component $w_s \langle \mathbf{e}_k^{\text{static}}, \mathbf{e}_q \rangle$ handles identity queries (“glass cup”), while the temporal component $w_t \max_f \langle \mathbf{e}_{k,f}^{\text{sync}}, \mathbf{e}_q \rangle$ handles state queries (“cup being filled”). Free-form queries that combine identity and state are naturally supported by the weighted mixture.

H.16 Appearance-Driven States

■ When state changes are driven by surface appearance rather than motion (chickchicken), the 28D kinematic vector carries little discriminative signal and the ridge map reduces to $\hat{\mathbf{e}}_{k,f} \approx \mathbf{e}_k^{\text{static}}$. Narrower margin ($\Delta\text{Acc} = +0.09$ vs. 4D LangSplat, compared to $+0.62$ on americano) reflects this directly. Fusing MLLM appearance features with kinematic features is a natural extension. Importantly, even on chickchicken the method does not *degrade* below baselines; it matches or exceeds them by relying on the static anchor when kinematic signal is absent.

H.17 SE(3) and Articulated Bodies

■ Shared SE(3) captures only the dominant rigid component; part-level articulation is absorbed into residuals and flagged by modulation ($m_i > 0.5$ on 23% of Gaussians, concentrated on expected regions: boundaries, joints, deforming surfaces). The modulation mechanism ensures these regions are not over-regularized: their residuals are permitted to be large, preserving reconstruction quality while still allowing the shared transform to capture the dominant motion component. Hierarchical part-based decomposition is a future direction.

H.18 Temporal Interpolation and the Per-Frame Table

■ The per-frame \mathcal{M}_ϕ table stores SE(3) parameters at observed timesteps only and does not natively interpolate to unseen times. This is a deliberate choice: the method targets within-sequence understanding (what happened, when, and to which object), not temporal super-resolution or future prediction. For within-sequence evaluation, all metrics are computed at training-frame timestamps, so interpolation is not required.

Should interpolation be needed (e.g., for slow-motion rendering between observed frames), two options exist without retraining: (i) linear interpolation in the SE(3) tangent space (SLERP for rotation, linear for translation) between adjacent stored frames, which is well-defined given the smoothness enforced by $\mathcal{L}_{\text{smooth}}$; (ii) the implemented MLP variant of \mathcal{M}_ϕ (§A.2), which takes continuous $\gamma(t)$ as input and produces transforms at arbitrary timesteps. The MLP variant was not used in reported experiments because it adds hyperparameter sensitivity without improving within-sequence metrics, but it is available for applications requiring continuous-time queries.

The $\mathcal{L}_{\text{smooth}}$ regularizer ensures that adjacent frames have similar transforms (first-order finite-difference prior), so the per-frame table is smooth by construction and interpolation between frames would produce physically plausible intermediate states.

H.19 SE(3) vs. Affine: When Each Variant Applies

■ Both SE(3) and affine parameterizations of \mathcal{M}_ϕ are implemented. SE(3) (6 parameters per object per frame: 3 rotation, 3 translation) is the default because it enforces rigid-body structure, which provides the strongest inductive bias and yields physically interpretable rotation/translation components that directly feed the 28D kinematic feature vector (dims 2, 16, 17).

The affine variant (12 parameters: 3×3 matrix delta + 3 bias) relaxes the rigidity assumption, allowing shear and anisotropic scaling. It is appropriate when objects undergo volume-changing deformations (e.g., inflating, compressing) that cannot be captured by rotation and translation alone. The cost is a weaker inductive bias: with more degrees of freedom, the affine transform can absorb motion that would otherwise remain in the residual, potentially reducing the interpretability of the factorization.

In our HyperNeRF experiments, the SE(3) variant was sufficient because the dominant object motions (pouring, lifting, splitting) are approximately rigid. For scenes with significant non-rigid object-level deformation, the affine variant or a combination (SE(3) for rigid objects, affine for deformable ones, selected per object) would be more appropriate. The modular \mathcal{M}_ϕ interface makes switching between variants a single configuration change with no architectural modifications.

H.20 Augmenting Kinematics with Appearance Features

■ The 28D kinematic feature vector is purely motion-derived. For appearance-driven state changes (e.g., chickchicken, where color/texture changes carry more signal than motion), augmenting the feature vector with low-dimensional appearance descriptors is a natural extension. Candidate features include: (i) mean RGB of the object crop (3D), (ii) color histogram in a compact basis (e.g., 8D), (iii) the first few PCA components of the SigLIP crop embeddings (capturing appearance variation orthogonal to the static anchor).

Such augmentation would expand the ridge-map input from 29D to approximately 35–40D while preserving the closed-form solution. The per-object standardization and ridge regularization ($\lambda = 0.01$) would prevent overfitting even with the additional dimensions, given that sample counts per object ($|\mathcal{F}_k| \approx 50\text{--}200$) substantially exceed the feature dimensionality.

This extension is fully compatible with the existing pipeline: it affects only the feature construction step in Phase 3 and requires no retraining of Phases 1–2. We expect the largest gains on scenes like chickchicken where the current narrower margin ($\Delta\text{tIoU} = +0.13$ vs. 4D LangSplat) reflects limited kinematic signal.

H.21 Neu3D Results

■ The main paper lists Neu3D as an evaluation dataset (6 multi-view dynamic scenes). Table S1 reports per-scene results for 4D SYNCHRONIZED FIELDS on Neu3D at 20k iterations, covering both reconstruction-only (Phase 1) and motion-factorized (Phase 2) stages.

We ran LangSplat and LEGaussians on all six Neu3D scenes using their official codebases under the same COLMAP initialization. LangSplat is a static 3D method with no deformation model; it produced training outputs but all test-time rendering on dynamic frames yielded degenerate images from which no valid PSNR, SSIM, or LPIPS could be computed. LEGaussians similarly lacks a temporal backbone and did not converge to valid test renderings. In both cases the failure is architectural (no mechanism to handle frame-to-frame motion), not an implementation error in our evaluation pipeline. We verified that both methods produce valid metrics on static 3D benchmarks using the same codebase.

4D SYNCHRONIZED FIELDS achieves 33.23 dB mean PSNR after motion decomposition, a +1.45 dB improvement over the reconstruction-only backbone (31.78 dB). This confirms, on a second dataset, that the motion factorization acts as a beneficial inductive bias rather than a reconstruction penalty, consistent with the HyperNeRF finding in the main paper (28.52 vs. 27.59 dB, +0.93 dB, Table 4 of the main paper). The Neu3D improvement is larger (+1.45 vs. +0.93 dB), likely because multi-view Neu3D scenes provide more geometric constraints for the per-object SE(3) transforms to exploit.

The mean rigid-share ratio ($\bar{\rho} = 0.879$) is substantially higher than on HyperNeRF ($\bar{\rho} = 0.472$), reflecting the fact that Neu3D scenes contain predominantly

Table S1: **Neu3D per-scene results for 4D Synchronized Fields** (20k iter). Phase 1: reconstruction-only backbone. Phase 2: with motion decomposition. $\bar{\rho}$: rigid-share ratio.

Scene	Recon-only (Phase 1)		+ Motion (Phase 2)		$\bar{\rho}$
	PSNR \uparrow		SSIM \uparrow		
	Ph. 1	Ph. 2	Ph. 1	Ph. 2	
Coffee Martini	30.44	31.71	.952	.956	.853
Cook Spinach	32.17	32.35	.960	.952	.885
Cut Roast. Beef	30.33	32.89	.957	.956	.908
Flame Salmon	30.24	31.34	.953	.957	.867
Flame Steak	32.43	33.81	.966	.965	.893
Sear Steak	35.05	37.27	.968	.971	.869
Mean	31.78	33.23	.959	.959	.879

rigid object manipulations (cutting, searing, pouring) with less non-rigid deformation than the HyperNeRF scenes.

All architecture, hyperparameters, and training schedules are identical to the HyperNeRF experiments; no per-scene or per-dataset tuning was applied.

I Failure Cases

F1: Systematic mask errors. Consistent mis-segmentation across all views propagates into incorrect transforms.

F2: Appearance-driven states. Kinematic features uninformative when state changes are visual, not motoric (chickchicken).

F3: Long occlusion. Embedding degrades to $\mathbf{e}_k^{\text{static}}$.

F4: Articulation. SE(3) captures dominant rigid component only; part-level motion absorbed into residuals.

F5: Scale ambiguity. Per-object standardization mitigates single-object features but not relational dims 20–27.

Foundation model biases (SAM 3, SigLIP) are inherited; relevant for safety-critical deployment.

J Broader Impact

The central premise of this work is that reconstruction, object-factored motion, and language are not independent problems to be solved in sequence but coupled aspects of a single representational challenge. By demonstrating that a lightweight in-loop factorization can expose interpretable motion primitives at negligible reconstruction cost, and that a closed-form linear map from those primitives to language embeddings more than doubles temporal localization

quality over post-hoc distillation baselines, the method provides empirical evidence that *motion structure is a viable and underexploited conditioning signal for semantic grounding in dynamic scenes.*

This finding points toward a broader research direction: building 4D representations in which every learned quantity (geometry, deformation, object identity, semantics) is structurally accessible to every other, rather than layered as frozen modules. The object-time language field, the kinematic feature interface, and the per-object ridge map are intentionally simple instantiations of this principle; stronger motion models, richer feature spaces, and tighter integration with world models and embodied planners are natural next steps that the modular architecture is designed to support.